VT/VF risk in animal model of hypertensive heart disease predicted by distribution of patchy fibrosis

Supplementary Material

Prashanna Khwaounjoo,[1,2] Gregory B. Sands,[1] Ian J. LeGrice,[1,3] Girish Ramulgun,[1] Anne M. Gillis,[4] Bruce H. Smaill,[1] Mark L. Trew[1]

[1]Auckland Bioengineering Institute, University of Auckland, Auckland, New Zealand; [2]Department of Anatomy, University of Otago, Dunedin, New Zealand; [3]Department of Physiology, University of Auckland, Auckland, New Zealand; [4]Libin Cardiovascular Institute of Alberta, University of Calgary, Calgary, AB, Canada.

S1. Introduction

This supplement provides additional methodological detail for new 2D analysis of fibrosis distributions in wheat germ agglutinin-conjugated AF488 (WGA) labeled cardiac tissue. It also describes 3D cell segmentation and analysis of confocal images from methyl salicylate cleared cardiac tissue. Finally, it includes results illustrating pre-block alternans observed in the different SHR age cohorts.

S2. Anatomical measurements and fibrosis distribution

Tiled images of WGA-labeled short axis sections of rat heart were combined with ImageJ (imagej.nih.gov) to create a single image. Figure S1A shows an example from an 18 month animal. Initial segmentation of tissue from non-tissue used a binary filter to obtain a mask for the short axis slice (Figure S1B). Measurements were taken of the average thicknesses of the LV and RV (Figure S1B) and lumen area and lumen centroid (Figure S1C).

Cell membranes and the ECM are labeled by WGA. Greater image intensity within the boundary mask indicates the presence of fibrosis (Figure S1A), while the spatial distribution of this signal provides information on the nature and extent of this fibrosis. Using a maximum entropy intensity filter[1] the higher intensity pixels were segmented to differentiate the regions of fibrosis from the rest of the tissue and create a mask (Figure S1D). This filter was chosen as it was able to duplicate the histogram based WGA fibrosis segmentation from Emde et al. (2014)[2]. For all hearts, the total segmented area of fibrosis was normalised with respect to short-axis area to determine the fibrotic percentage.

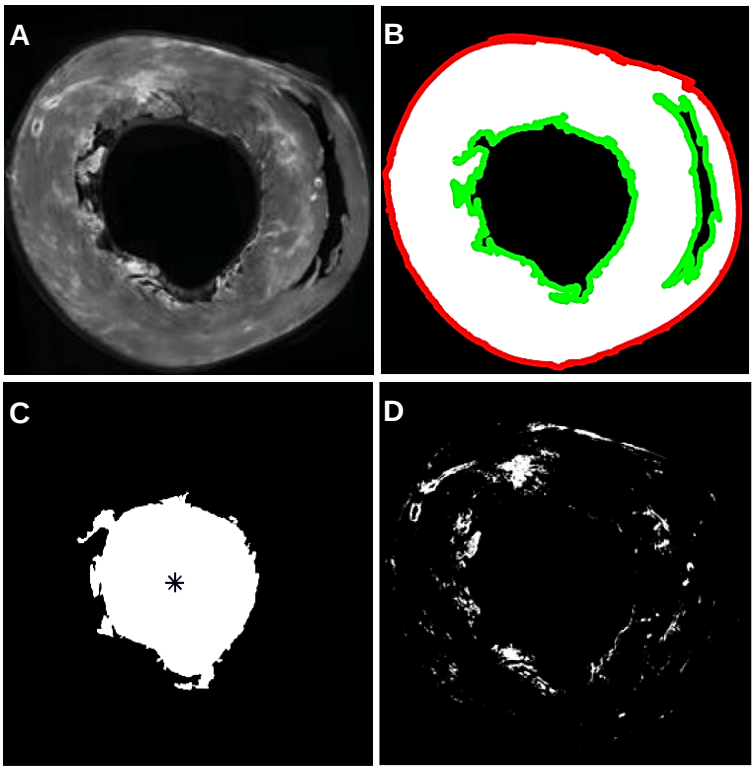

Figure S1. Short axis slice representation and measurements. **A.** Merged WGA stained short axis slice (higher intensity pixels indicate fibrosis) **B.** Tissue segmentation (white), endocardial (green) and epicardial (red) coordinates **C.** LV cavity with centroid highlighted by asterisk. **D.** Segmented patches of fibrosis.

To quantify and compare the distribution of fibrosis across all hearts, the segmented mask (Figure S1D) was translated into a polar coordinate system. For each separate individual patch in the mask (i.e. a patch of fibrosis – based on the WGA intensity signal), the patch centroid and area were computed. The centroid position was mapped into a polar coordinate system based on its polar angle and transmural (wall thickness) location relative to the lumen centroid (Figure S2A). A polar angle of 0^{o} was defined as mid septum and 90^{o} to 270^{o} were the LV free wall. In the transmural field 0 was the endocardium and 1 the epicardium. Local "densities" of the patches were then determined by discretizing the spatial field into 50 by 50 bins. The resultant field was smoothed using a 2D histogram filter[3] to create a "heat map" (Figure S2B).

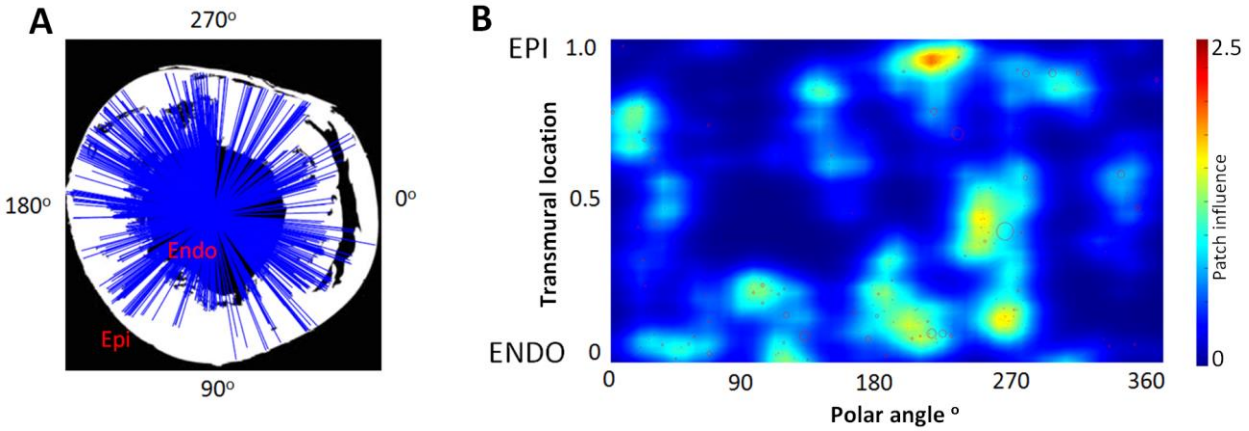

Figure S2. Fibrosis patch distribution and density. **A.** Intramural location of patches of fibrosis relative to LV cavity centroid. Blue lines indicate identification of patch from cavity centre. **B.** Heat map of fibrosis patch density in the polar coordinate system. Colour scale indicates influence of patch of fibrosis. Red indicates the influence of 2.5 or more patches and dark blue indicates no fibrotic influence.

The heat map was resampled to 100×360 pixels in the transmural and polar angle axes respectively. A threshold (using a value of 1, representing the influence of one patch) was applied to the resampled "heat map" image to quantify the influence of fibrosis patch density and extract the connected high-density regions. These aggregated regions of fibrosis patches from the heat map in Figure S2B are shown in Figure S3A as white regions. The regions were skeletonized, using the MATLAB® `bwskel`* function, as shown in Figure S3B and Figure S3C. The area of the region with the longest skeletonization (a measure of fibrotic patch density tortuosity and, hence, possible reentrant path length – referred to as the aggregated fibrosis patch density length (AFL)) was normalized across all hearts in the study giving an index between 0 and 1. This is the aggregated fibrosis patch density area (AFA) index.

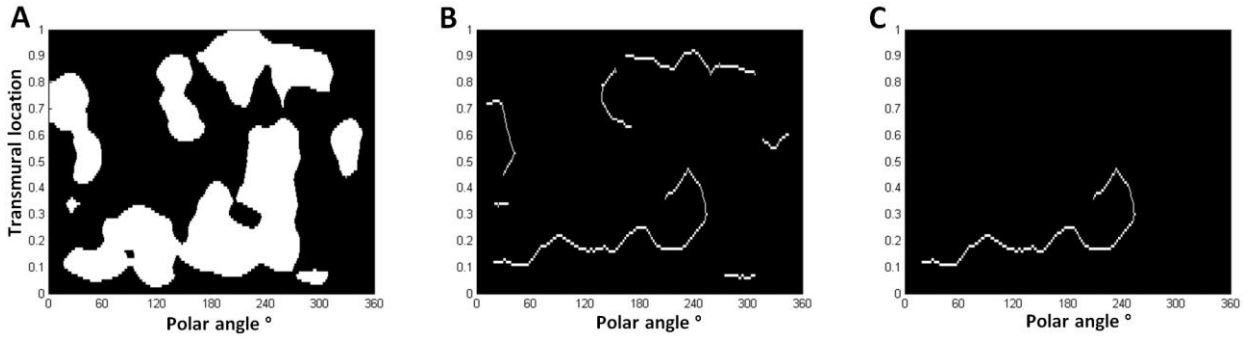

Figure S3. Mask of connected regions of fibrosis and measurements. **A.** Mask of connected regions of fibrosis (threshold of 1) **B.** Skeletonised lengths of each separate contiguous region of the mask **C.** Maximum path length of the skeletonised lengths.

This method for assessing the aggregation of fibrosis patch density in cardiac tissue ensures that the structure of the fibrotic patch distribution is correctly accounted for. Fibrotic structures as barriers to coordinated activation would not be fully captured by just a maximum area measure,

* mathworks.com/help/images/ref/bwskel.html

for example. Our fibrotic consolidation measure includes both path length and area, and holds similarities to a measure of tortuosity in 2D discontinuous myocardium that was developed and used in the analysis of Engelman et al. (2010).[4]

Typical examples of the spatial distributions and characteristics of fibrosis quantified using this method applied to LV short axis slices are shown in Figure S4. The dark areas in Figure S4A are regions of intense WGA fluorescence due to perimysial or replacement fibrosis. The heterogeneous distribution of these patches is highlighted in the polar distribution maps (Figure S4B) and the analysis of fibrotic regional connectedness is shown in Figure S4C.

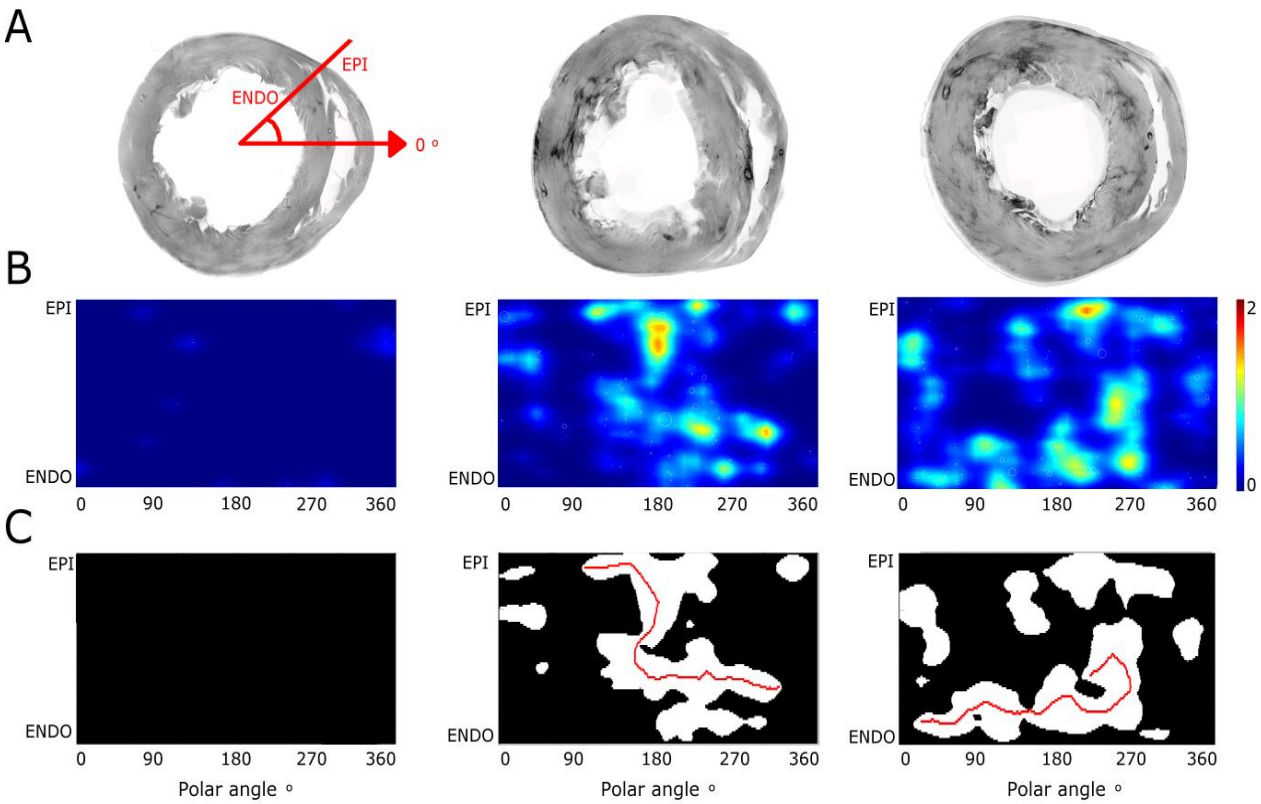

Figure S4. Typical distributions of WGA staining in LV short-axis sections at 6, 12 and 18 months. **A.** Initial LV sections, intensely dark regions stained are representative of patches of fibrosis. **B.** Polar heat maps reflect the intensity and regional extent and the distribution of patches of fibrosis. **C.** Characterisation of potentially connected regions of fibrosis (white). Maximum skeletonised lengths are indicated in red.

Each high intensity pixel (darker pixels in Figure S4A) was also translated into the polar coordinate field to quantify the distribution of the amount of fibrosis. The resulting image was discretized into 10 and 12 segments for the transmural and polar axes respectively (Figure S5).

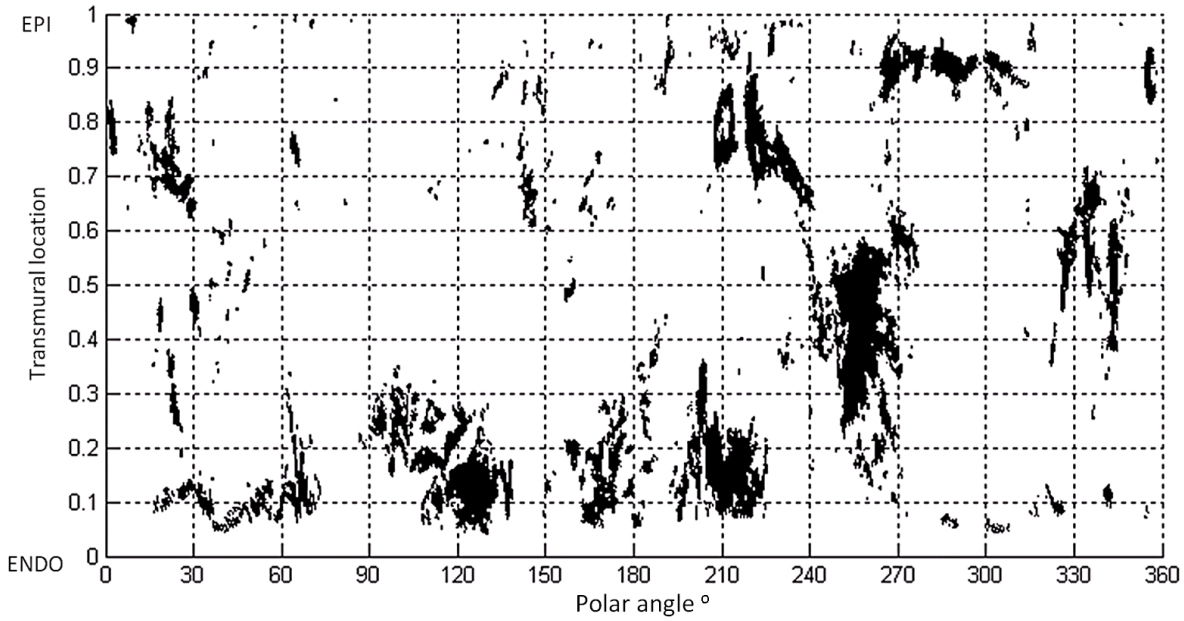

Figure S5. Distribution of fibrosis (individual high intensity pixels of WGA) in circumferential and transmural coordinate system. Transmural axes discretised into 10 sections of 0.1 units, while the circumferential axes have been discretised into 12 radial sections of 30 °. These data are equivalent to data in figures S1, S2, S3 and S4 column 3.

S3. Cellular organization and architecture

ITK SNAP (itksnap.org) [5] was used to manually segment the high resolution cell data into individual cells (Figure S6). The segmentation was conducted by a contract operator with no link to the project and its potential findings (i.e. they were unaware of potential alterations to cell morphology with HHD progression). For each internal cell (i.e. a whole myocyte fully contained in the image volume) the longitudinal orientation was determined using the eigenvectors of the covariance matrix [6]. The longitudinal axis and centre of mass of the cell were then used to determine the cell cross sectional area. Cell lengths and total cell volumes were also measured, while the surface areas were calculated using Minkowski measures[7]. Distance maps from each internal (whole) myocyte were generated to identify/count all other myocytes within a distance of 1 voxel (0.41 μm) to the outer sarcolemma. This metric was used to provide an estimate of likely cell coupling i.e. number of neighboring myocytes. The relative volume of the fibrosis was estimated from the WGA intensity using the ImageJ (imagej.nih.gov) implementation of the Shanbhag filter.

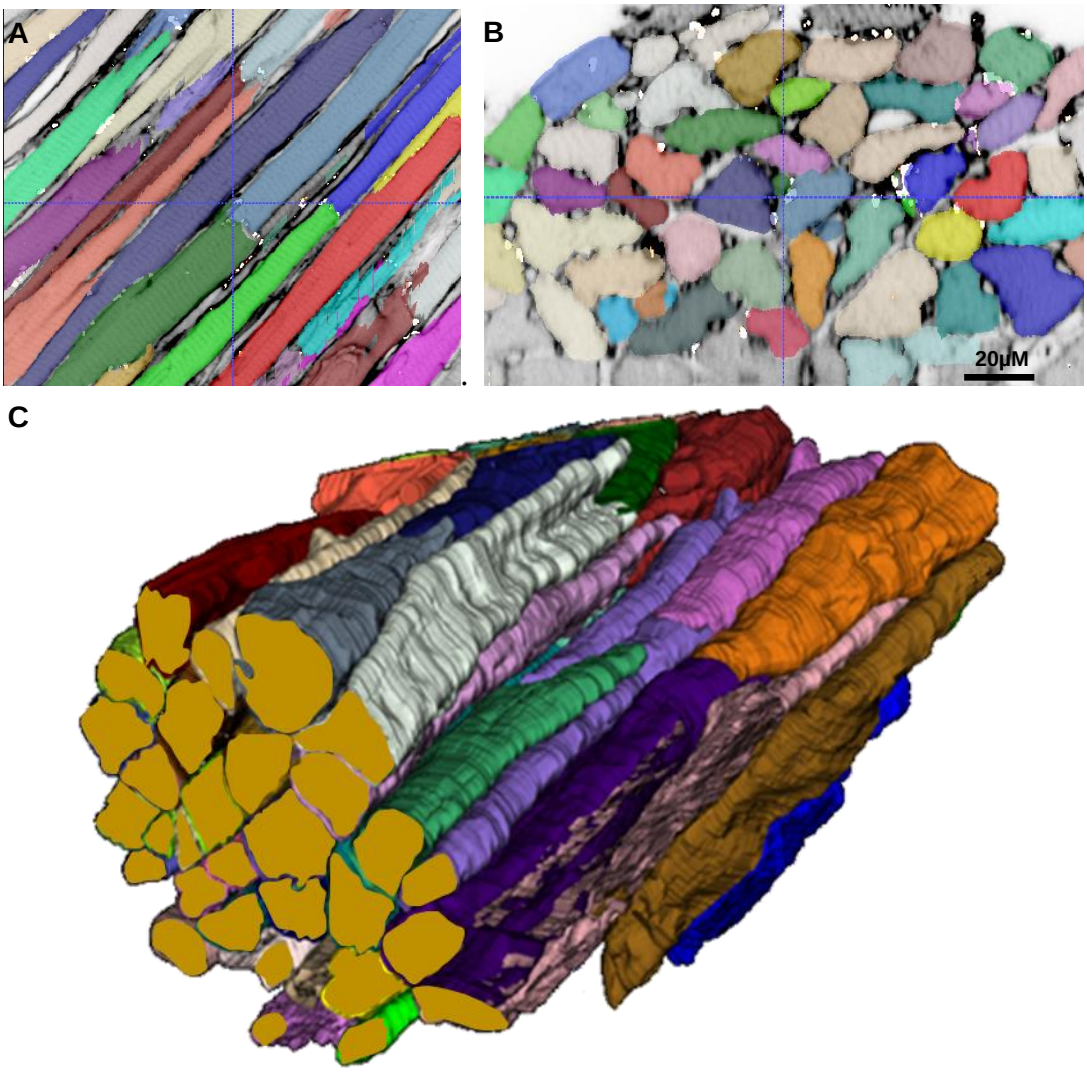

Figure S6. Cell segmentations using ITK SNAP. **A.** Axial slice of tissue volume. **B.** Side view of tissue section. **C.** 3D redering of segmented cells. Cells not wholly in the image volume are identified by their truncation at the image boundaries.

S4. Induction and duration of arrhythmia

Ventricular tachycardia or ventricular fibrillation (> 5 s duration) was induced in 17% of 6 month, 83% of 12 month and 100% of 18 month cohorts. The median duration of arrhythmia induced in 6 month SHRs was 3.7 s, in 12 month 11.7 s and in 18 month 43.4 s.

S5. Rate dependent alternans

In all animals, 1:1 capture failed as the pacing rate increased and 2:1 block occurred. Over a range of base cycle lengths (BCL) prior to loss of 1:1 capture, alternans rhythm was observed in optical action potential amplitudes for all animals and activation times for most animals. Table S1 summarizes the BCL thresholds and the observed nature and prevalence of alternans. Figures S7 to S9 illustrate alternans rhythms in 6, 12 and 18 month rats, respectively. Overall, animals displaying discordant activation time (AT) alternans prior to loss of capture had significantly higher arrhythmic risk (8.1±4.1; $p < 0.005$) compared to animals showing concordant or no AT alternans (3.9±4.1). Animals with discordant AT alternans were associated with a significantly higher patchy fibrosis index (0.2±0.1) compared to animals displaying concordant AT alternans (0.07±0.09; $p < 0.05$) and animals displaying no AT alternans (0.02±0.02; $p < 0.05$).

Table S1. Summary of observed alternans onset conditions and categorization. BCL: base cycle length of pacing; AMP: amplitude; AT: activation time.

	6 month (n=6)	12 month (n=6)	18 month (n=5)
Conduction block	BCL < 129±10 ms	BCL < 145±21 ms	BCL < 136±14 ms
Observed alternans	BCL < 139±9 ms	BCL < 165±21 ms	BCL < 161±14 ms
Discordant AMP alternans (% animals)	100	100	100
No AT alternals (% animals)	50	0	0
Concordant AT alternans (% animals)	33	67	40
Discordant AT alternans (% animals)	17	33	60

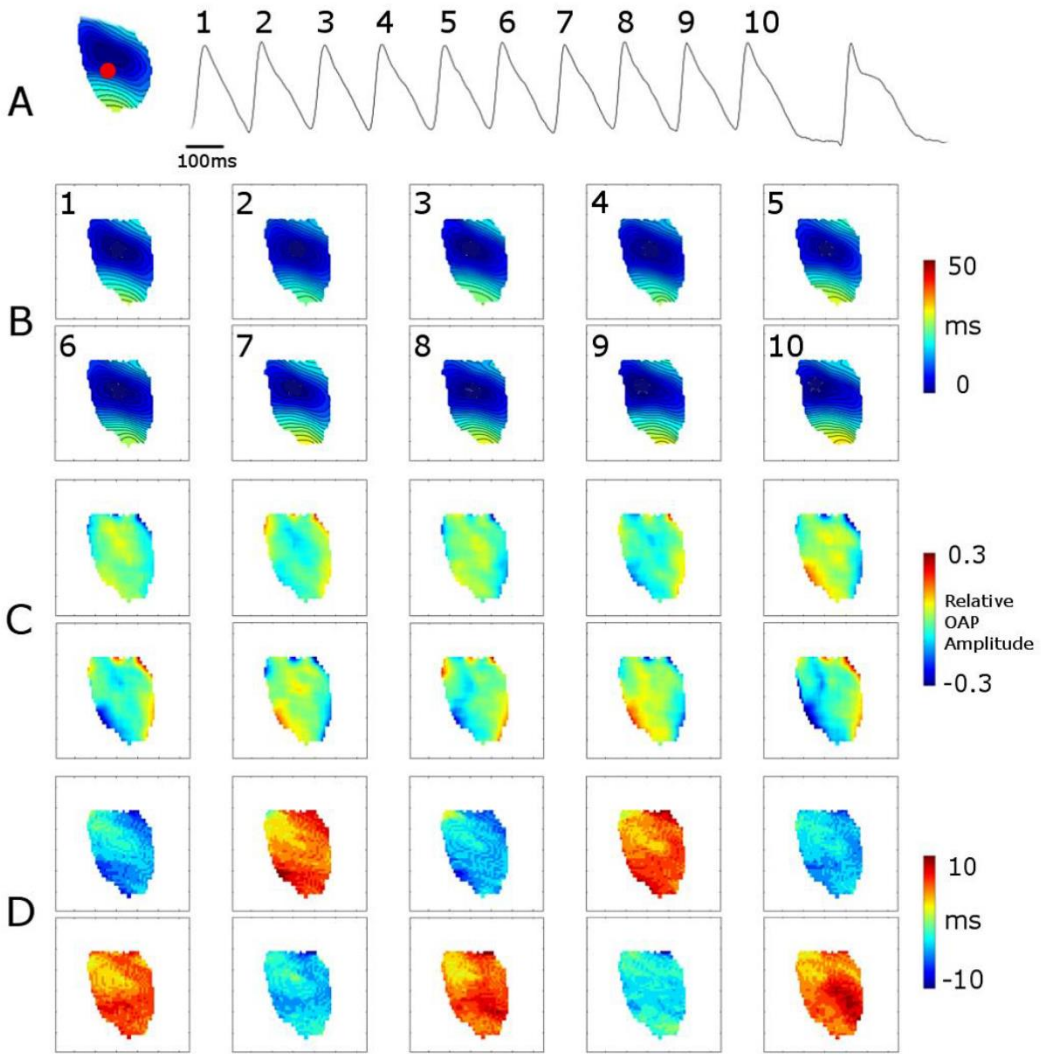

Figure S7. Activation and alternans rhythm observed in 6 month SHR over 10 beats prior to 2:1 block for BCL of 122 ms. **A.** Optical action potential trace at indicated site on the LV free wall. **B.** Activation time sequence for each of 10 beats. 2 ms isochrones. **C.** Optical action potential (OAP) discordant alternans shown by relative difference between current and previous beat. **D.** Activation time concordant alternans shown by difference between current and previous beat.

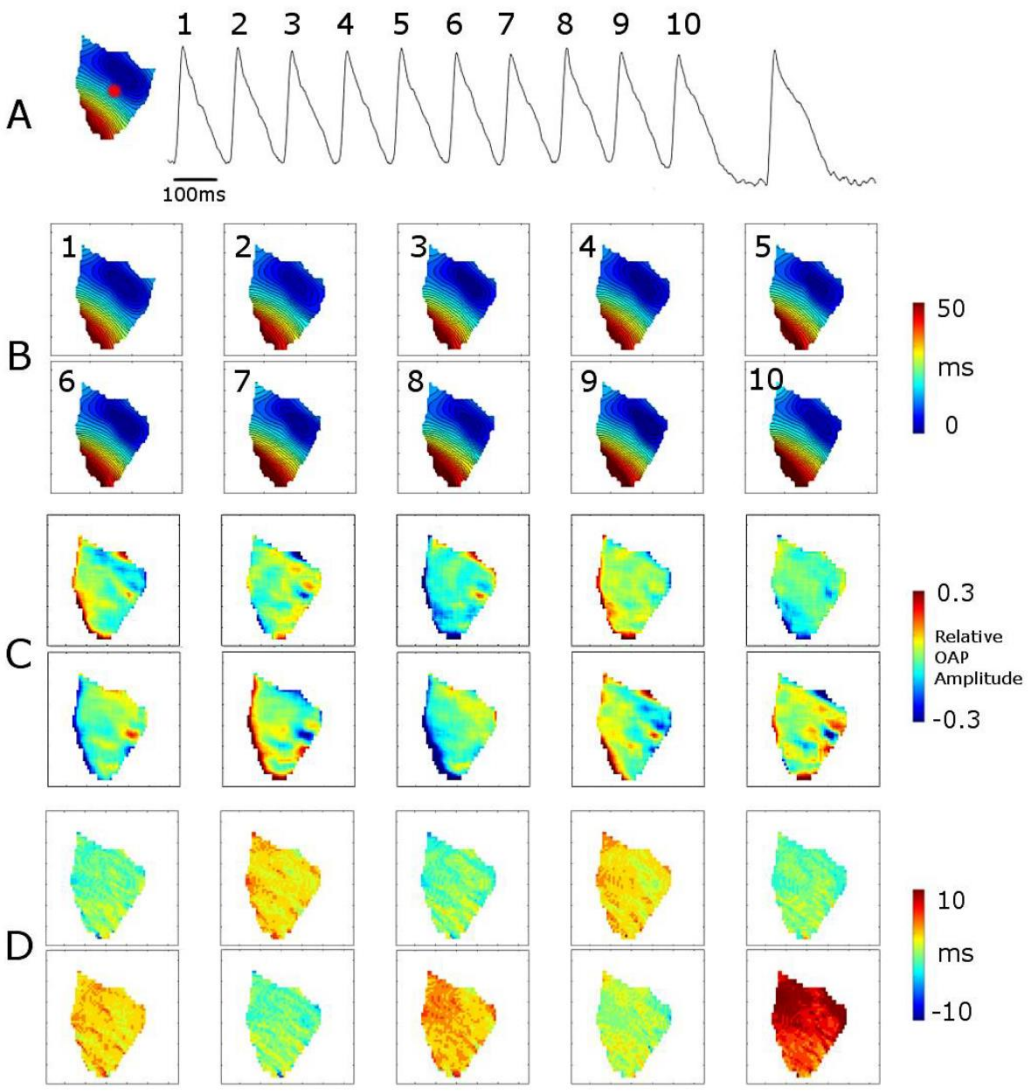

Figure S8. Activation and alternans rhythm observed in 12 month SHR over 10 beats prior to 2:1 block for BCL of 143 ms. **A.** Optical action potential trace at indicated site on the LV free wall. **B.** Activation time sequence for each of 10 beats. 2 ms isochrones. **C.** Optical action potential (OAP) discordant alternans shown by relative difference between current and previous beat. **D.** Activation time concordant alternans shown by difference between current and previous beat.

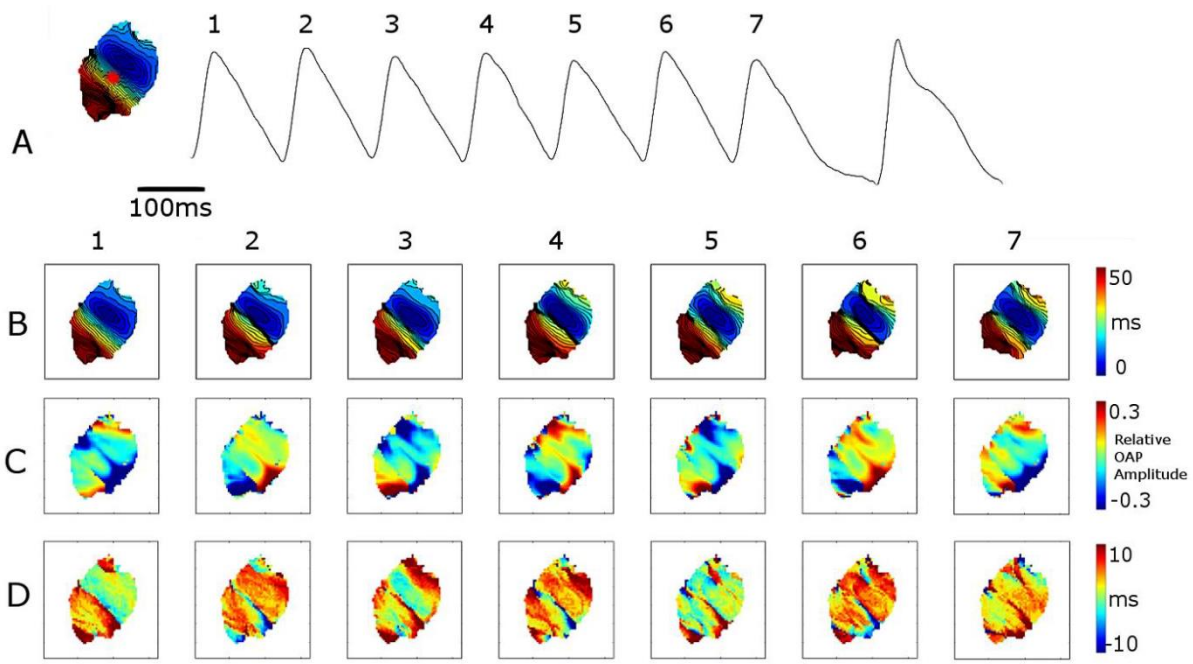

Figure S9. Activation and alternans rhythm observed in 18 month SHR over 7 beats prior to 2:1 block for BCL of 139 ms. **A.** Optical action potential trace at indicated site on the LV free wall. **B.** Activation time sequence for each of 7 beats. 2 ms isochrones. **C.** Optical action potential (OAP) discordant alternans shown by relative difference between current and previous beat. **D.** Activation time discordant alternans shown by difference between current and previous beat.

S6. Global LV morphology

Closed contours were fitted to the inner and outer LV surfaces of the composite WGA confocal images of short-axis rings. The images were acquired using a Nikon TE2000 inverted confocal microscope system (excitation wavelength 488 nm; 4× objective: NA 0.13, WD 16.4 mm; 6.22 × 6.22 μm^2 pixels). Areas bounded by both contours were determined, as well as the estimated total LV wall cross-section area, average inner and outer diameters and wall thickness for equivalent circular contours. The dimensions from the center of the inter-ventricular septum (IVS) to the center of the LV free wall (Figure S10) and the LV wall thickness at the center of LV free wall were also calculated. The results are given in Table S2 and the short axes slices for all animals across all cohorts are given in Figure S10. The measured dimensions align with expectation of increasing wall thickness from 6-12 months and then decreasing again in the 18 month animals. Simple statistics suggest that changes in wall thickness are real but mostly non-significant.

Table S2. Global LV morphology of short-axis sections across age cohorts. *p<0.05 for one tailed test.

	6 month (n=6)	12 month (n=6)	18 month (n=5)
Wall area (mm^2)	82.96±10.56	92.80±8.89	82.96±13.86
Average outer diameter (mm)	12.87±1.05	13.40±0.59	13.14±0.96
Average inner diameter (mm)	7.68±1.50	7.79±1.09	8.20±0.88
Average wall thickness (mm)	2.59±0.39	2.81±0.37	2.47±0.34
LV freewall wall thickness (mm)	2.71±0.48	3.18±0.59*	2.60±0.27*
Distance IVS to LV freewall (mm)	7.34±1.95	7.29±1.32	7.59±0.97

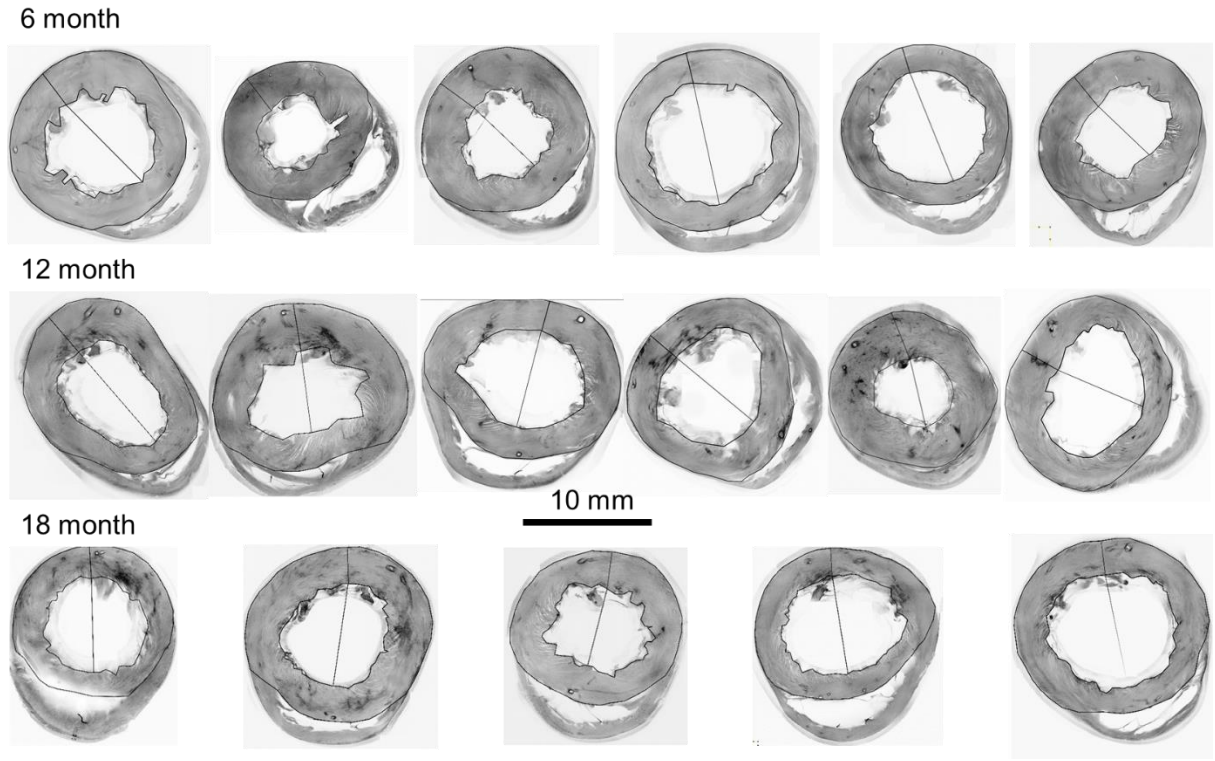

Figure S10. Short axis sections from all hearts with inner and outer diameter contours shown, together with LV freewall thickness and distance from IVS to LV freewall.

S7. References

1. Zheng X, Ye H, Tang Y. Image Bi-Level Thresholding Based on Gray Level-Local Variance Histogram. *Entropy*. 2017;19:191.
2. Emde B, Heinen A, Gödecke A, Bottermann K. Wheat germ agglutinin staining as a suitable method for detection and quantification of fibrosis in cardiac tissue after myocardial infarction. *Eur J Histochem*. 2014;58:2448.
3. Eilers PHC, Goeman JJ. Enhancing scatterplots with smoothed densities. *Bioinformatics*.

2004;20:623–628.
4. Engelman ZJ, Trew ML, Smaill BH. Structural heterogeneity alone is a sufficient substrate for dynamic instability and altered restitution. *Circ Arrhythm Electrophysiol*. 2010;3:195–203.
5. Yushkevich PA, Piven J, Hazlett HC, Smith RG, Ho S, Gee JC, Gerig G. User-guided 3D active contour segmentation of anatomical structures: Significantly improved efficiency and reliability. *Neuroimage*. 2006;
6. Reyment RA, Jvreskog KG. Applied Factor Analysis in the Natural Sciences. 1993.
7. Legland D, Kiêu K, Devaux M-F. Computation of minkowski measures on 2D and 3D binary images. *Image Anal Stereol*. 2011;26:83.